Biomimetic engineering of the cardiac tissue through processing, functionalization, and biological characterization of polyester urethanes

Federico Vozzi[1] , Federica Logrand[2], Manuela Cabiati[1], Claudia Cicione[3], Monica Boffito[4], Irene Carmagnola[4], Nicoletta Vitale[2], Manuele Gori[3], Mara Brancaccio[2], Silvia Del Ry[1], Dario Gastaldi[5], Emanuele Cattarinuzzi[5], Pasquale Vena[5], Alberto Rainer[3], Claudio Domenici[1], Gianluca Ciardelli[4] and Susanna Sartori[4]

[1] Institute of Clinical Physiology, IFC-CNR, Via Moruzzi 1, I-56124 Pisa, Italy
[2] Department of Molecular Biotechnology and Health Sciences, University of Turin, Via Verdi 8, I-10124 Turin, Italy
[3] Università Campus Bio-Medico di Roma, Via Álvaro del Portillo 21, I-00128 Rome, Italy
[4] Department of Mechanical and Aerospace Engineering, Polytechnic of Turin, Corso Duca degli Abruzzi 24, I-10129 Turin, Italy
[5] Department of Chemistry, Materials and Chemical Engineering 'Giulio Natta', Politecnico di Milano, Piazza Leonardo da Vinci 32, I-20133 Milan, Italy

E-mail: vozzi@ifc.cnr.it

Keywords: polyurethane, cardiac tissue engineering, cardiomyocytes, biomimetic, scaffold, phenotypic modulation

Abstract

Three-dimensional (3D) tissue models offer new tools in the study of diseases. In the case of the engineering of cardiac muscle, a realistic goal would be the design of a scaffold able to replicate the tissue-specific architecture, mechanical properties, and chemical composition, so that it recapitulates the main functions of the tissue. This work is focused on the design and preliminary biological validation of an innovative polyester urethane (PUR) scaffold mimicking cardiac tissue properties. The porous scaffold was fabricated by thermally induced phase separation (TIPS) from poly(ε-caprolactone) diol, 1,4-butanediisocyanate, and L-lysine ethyl ester. Morphological and mechanical scaffolds characterization was accomplished by confocal microscopy, and micro-tensile and compression techniques. Scaffolds were then functionalized with fibronectin by plasma treatment, and the surface treatment was studied by x-ray photoelectron spectroscopy, attenuated total reflectance Fourier transform infrared spectra, and contact angle measurements. Primary rat neonatal cardiomyocytes were seeded on scaffolds, and their colonization, survival, and beating activity were analyzed for 14 days. Signal transduction pathways and apoptosis involved in cells, the structural development of the heart, and its metabolism were analyzed. PUR scaffolds showed a porous-aligned structure and mechanical properties consistent with that of the myocardial tissue. Cardiomyocytes plated on the scaffolds showed a high survival rate and a stable beating activity. Serine/threonine kinase (AKT) and extracellular signal-regulated kinases (ERK) phosphorylation was higher in cardiomyocytes cultured on the PUR scaffold compared to those on tissue culture plates. Real-time polymerase chain reaction analysis showed a significant modulation at 14 days of cardiac muscle (MYH7, prepro-ET-1), hypertrophy-specific (CTGF), and metabolism-related (SLC2a1, PFKL) genes in PUR scaffolds.

Introduction

Cardiovascular disease (CVD) is one of the major causes of death in the world, and the set of related pathologies, as hypertension, heart failure, and atherosclerosis, represents a huge cost for healthcare systems [1, 2]. Several approaches to contrast these diseases have been studied, and new therapies in terms of drugs, medical devices, and surgical solutions have been developed. One of the newest supports to study CVD physiopathology is the *in vitro* three-dimensional (3D) model, which can replicate the cardiac structure by definition of tissue-specific architecture and mechanical properties [3, 4], and mimic the myocardial extracellular matrix (ECM) through the

incorporation of ECM molecules (e.g. laminin, fibronectin, and collagen). This approach can ensure that a 3D model is able to support cardiac cell attachment and function [5].

Currently, the cell culture platforms for studying cardiac physiology are systems based on the following: (i) hydrogels, mainly constituted by ECM proteins such as collagen, fibrin, and matrigel, organized as ring- or strip-shaped microtissues with aligned cells (namely, engineered heart tissues (EHT)); (ii) self-organized cell aggregates made of cardiac stem cells (namely, organoids); and (iii) pre-fabricated scaffolds, generally made of synthetic biocompatible polymers, with a well-defined structure in terms of fiber alignment and porosity. Each one has specific advantages and limitations. EHTs show a high biocompatibility through the use of natural polymers, but present limited mechanical properties and low oxygen/nutrients diffusion [6]. Organoids are able to form compact tissue-like systems with a strong cell–cell interaction, and are able to mimic cardiac physiology [7]; however, their main limitation is their small size, which creates a diffusion barrier for oxygen and nutrients [8]. Lastly, 3D scaffolds obtained with synthetic polymers, such as polyurethanes, can be designed to recapitulate the architecture of the native tissue in terms of structure and mechanical properties [9]. In some cases their drawbacks are unfavorable tissue responses, such as inflammation and initiation of the foreign body reac-tion due to polymer degradation products (e.g. aro-matic diammines derived from aromatic diisocyanate)[10], and material surface properties (hydrophobicity and the absence of biomolecules that interact with cell receptors) [11].

Cardiac muscle shows a Young's modulus of about 10–20 kPa at the diastole initial stages (strain $< 10\%$) that increases up to 50 kPa in healthy myocardium and 200–300 kPa in failing heart at the diastole end (strain $\approx$ 15%–22%) [12]. Cardiac tissue tensile stress and strain are in the ranges of 3–15 kPa [12] and 22%–90% [13], respectively. Furthermore, scaffolds for cardiac tissue engineering have to bear the contractile and expansive forces produced at each cardiac cycle. For this purpose, scaffolds with elastomeric properties are more suitable: elastomeric polymers, such as polyurethanes, may serve as appropriate raw materials [14].

The scaffold's requirements also include an appropriate porosity (to drive cell colonization and attachment, and to facilitate the exchange of nutrients, mainly oxygen and metabolites) and hierarchical structure (pore orientation and anisotropy) [12, 15]. The adult mammalian heart is composed of several cell types, the most abundant being cardiomyocytes, fibroblasts, and endothelial cells. Since cardiomyocytes, fibroblasts, and endothelial cells have dimensions in the of ranges 10–100 μm, 10–15 μm, and 8–12 μm, respectively, the scaffold pore size should be between tens to hundreds of micrometers [16]. The myocardium bears mechanical loads along a preferred direction [17]; this property results in an anisotropic structure characterized by fiber alignment along the direction of the applied stresses. Scaffolds with control of fiber alignment can be obtained by electrospinning onto a rotating mandrel or by excimer laser ablation; how-ever, these techniques have some limitations in terms of pore size [16] or correct connectivity [18]. Thermally induced phase separation (TIPS) has been employed to fabricate oriented scaffolds. This technique allows pore size and morphology tuning to be achieved by modulat-ing polymer concentration, quenching temperature, thermal gradient, and solvent type [16]. Fiber alignment supports cardiomyocytes in the generation of a tissue-like structure also acting on cell function in terms of cal-cium handling, action potentials, and conduction velo-cities, thus influencing the cardiac maturation in neonatal cardiomyocytes [19, 20] and the differentiation process in human embryonic stem cells [21].

As previously stated, in addition to the morphology and mechanical properties described above, an effective cardiac model should incorporate growth factors, ECM proteins (i.e. laminin, fibronectin, and collagen) or their epitopes (i.e. Arg-Gly-Asp peptide, Ile-Lys-Val-Ala-Val peptide, and Tyr–Ile–Gly–Ser–Arg peptide sequences). Regarding ECM proteins, fibronectin content is important for cardiac tissue engineering since it influences cell growth, development, integration, adhesion, cytoskeletal organization, and tissue remodeling [22, 23]. In our previous work [24] we developed a family of biodegradable polyester urethanes (PURs). In these series, the most promising polymer for muscle tissue engineering (due to its low Young's modulus and elastomeric behavior) was that synthesized from poly(ε-caprolactone) (PCL) diol (Mn $=$ 2000 g mol^{-1}), 1,4-butanediisocyanate (BDI), and L-lysine ethyl ester. This PUR was also used to obtain porous scaffolds by TIPS [25]. The PUR scaffolds turned out to be suitable for cardiac tissue engineering since their mechanical and structural properties at both the macro- and nano-scale were in accordance with the properties required for this application. The PUR was synthesized with the same building block described above (PCL diol (Mn $=$ 2000 g mol^{-1}), BDI, and L-lysine ethyl ester), and was processed by TIPS to produce porous scaffolds. Scaffold functionalization was performed by plasma treatment with acrylic acid, which led to the formation of a polyacrylic acid layer, followed by the activation of carboxylic groups and the grafting of fibronectin. Plasma surface modification was conducted to alter surface chemical functionalities of the scaffold without affecting bulk properties [26]. Cardiomyocytes constitute one-third of the cells in the myocardium (80%–90% of the total volume) [27], representing the

key cell source to develop and validate cardiac models. Primary neonatal cardiomyocytes deriving from Sprague–Dawley rats were allowed to seed on the biomimetic scaffold, and their adhesion, beating, and survival were analyzed. Moreover, signal transduction pathways involved in cell survival (extracellular signal-regulated kinases (ERK)1/2 and serine/threonine kinase (AKT)), as well as genes involved in apoptosis (Bcl2-associated X protein, B-cell CLL/lymphoma), structural development (natriuretic peptides system, endothelin-1, actin alpha cardiac muscle 1, myosin heavy chain 7, myosin heavy chain 6, troponin I type 3, connective tissue growth factor), and the balance between glucose and fatty acid metabolism (glucose transporter 1, phosphofructokinase, glucokinase regulator, pyruvate dehydrogenase kinase, isozyme 4, peroxisome proliferator-activated receptor δ, peroxisome proliferator-activated receptor α, peroxisome proliferator-activated receptor γ, coactivator 1 α), were analyzed and compared to cardiomyocytes seeded on tissue culture plates (TCP).

Methods

Materials

Poly(ε-caprolactone) diol (Mn = 2000 g mol^{-1}), dibutyltindilaurate (DBTDL), triethylamine, L-lysine ethyl ester dihydrochloride, 1-ethyl-3-(3-dimethylaminopropyl) carbodiimide, and N-hydroxysuccinimide were purchased from Sigma-Aldrich, USA. 1,4-butanediisocyanate was purchased from Molekula, Italy, and distilled under reduced pressure before use. In order to remove the residual water, poly(ε-caprolactone) diol and L-lysine ethyl ester dihydrochloride were dried overnight under reduced pressure at 100 °C and 40 °C, respectively. The glassware used in PUR synthesis was also dried under reduced pressure at 100 °C overnight. All solvents were purchased by Sigma-Aldrich (Italy) in the analytical grade. 1,2-dichloroethane (DCE) was stored over activated 4 Å molecular sieves under a nitrogen atmosphere for at least 24 h before use in order to reduce the water content below 20 ppm. Fibronectin (human) was purchased by YO Proteins (YO Proteins AB, Sweden).

Synthesis of PURs

PCL was dissolved in DCE and azeotropically dried by refluxing under nitrogen over molecular sieves for at least 8 h. BDI was then added to the solution (2:1 molar ratio with respect to PCL diol), and reacted with the macrodiol in the presence of the catalyst (DBTDL) to form the pre-polymer. At the end of this first step (150 min, 80 °C), the L-lysine ethyl ester dihydrochloride was dissolved in anhydrous DCE and added at a 1:1 molar ratio with respect to the macrodiol at room temperature. Triethyla-mine was also added to induce chain extender (L-lysine ethyl ester) neutralization. The chain extension reaction was stopped after 16 h by addition of methanol. The polymer was then collected by precipitation in petroleum ether and purified by dissolution in dimethylformamide followed by precipitation in methanol. The dissolution-precipitation step was repeated twice. Finally, the polymer was dried under vacuum at 60 °C for 24 h.

Scaffolds production

PUR was processed into scaffolds by TIPS according to the following procedure. The polymer was dissolved in dimethyl sulfoxide (DMSO ACS Reagent, Sigma-Aldrich, Italy) (8% w/v) at 50 °C. The solution was poured in parallelepiped stainless steel molds (50 mm × 25 mm × 30 mm) and quenched at −80 °C for 3 h. The frozen solution was then washed in ethanol/water (70/30 v/v) for three days, and finally lyophilized.

Scaffolds functionalization

Cylindrical scaffolds (8 mm diameter, 2 mm thickness) were obtained by cutting the specimens after freezing in liquid nitrogen. Argon plasma activation was performed in a plasma reactor (Pico, Diener Electronic, Germany) operating at a gas pressure of 0.7 mbar and a power of 70 W. The plasma treatment time was 60 s. Thereafter, acrylic acid vapors were allowed to flow in the process chamber until the final pressure of 0.05 mbar was reached; the plasma treatment was performed for 15 min. The scaffolds were then washed with distilled water three times to remove unreacted monomers. We will refer to these scaffolds as PUR-PAA. Fibronectin immobilization was performed according to the following protocol. PUR-PAA scaffolds were placed in 5 mg ml^{-1} of an aqueous solution (pH 5.0) of 1-ethyl-3-(3-dimethylaminopropyl) carbodiimide in the presence of 1.25 mg ml^{-1} N-hydroxysuccinimide at 4 °C for 20 h, washed, and immersed in fibronectin solution at 4 °C for 20 h. Concentration and pH of the fibronectin solution were 100 mg ml^{-1} and 5.0, respectively. Scaffolds were finally washed three times with distilled water to remove not covalently bound protein. We will call these scaffolds PUR-PAA-fibronectin; only this type of scaffold was tested for biological evaluation.

Infrared spectroscopy

Attenuated total reflectance Fourier transform infrared spectra (ATR-FTIR) of PUR was obtained at room temperature in the spectral range of 4000 to 400 cm^{-1} using a PerkinElmer Spectrum 100 equipped with an ATR accessory (UATR KRS5) with diamond crystal. The spectra, obtained as a result of 16 scans with a resolution of 4 cm^{-1}, were analyzed using the PerkinElmer Spectrum software. The same procedure was used to analyze the surface of PUR, PUR-PAA, and PUR-PAA-fibronectin scaffolds, but with a germanium accessory instead of a diamond one.

Molecular weight and distribution: size exclusion chromatography (SEC) analysis

PUR number-average and weight-average molecular weights (M_n and M_w), and molecular weight distributions (M_w/M_n), were estimated by SEC (1200 Series, Agilent Technologies, Santa Clara, CA, USA). The instrument was equipped with a refractive index detector and two Waters Styragel columns (HT2 and HT4) conditioned at 35 °C. Tetrahydrofuran (THF; inhibitor free, for high-performance liquid chromatography, 99.9%; Sigma-Aldrich, Italy) was used as the mobile phase at a flow rate of 0.5 ml min^{-1}. M_n and M_w were determined by the Agilent ChemStation Software relative to the universal calibration curve. The latter was constructed based on ten narrow polystyrene standards ranging in M_n from 740 to 18×10^4 g mol^{-1}. PUR was dissolved in THF (2 mg ml^{-1}) and filtered through a 0.45 μm syringe filter (Whatman) before analysis.

X-ray photoelectron spectroscopy (XPS)

XPS and electron spectroscopy for chemical analysis were performed with a PHI 5000 Versa Probe Instrument (Physical Electronics, Chanhassen, MN, USA) in a high vacuum chamber at a power of 25.6 W and voltage of 23.5 eV, with a scanning area of 500 × 500 μm^2. Analysis of XPS spectra was performed using XPSPEAK 4.1 software. The aliphatic carbon (C–C, C–H) at a binding energy of 285 eV (C 1 s photoline) was used to determine the charging.

Morphological characterization

To quantitatively assess the scaffold's porosity and wall thickness, confocal laser scanning was performed using a confocal laser microscope LEXT400 (Olympus).

The scans were performed on 80 μm thick samples, which were obtained by sectioning samples kept at low temperature and fixed on glass slides by means of a viscous fluid (killik, Bio-Optica). Sections were made by means of a criotome (HM 525, MICROM). All sections were deposited on a slide and let the killik evaporate.

The images where taken using a 20× objective lens, and six adjacent images were stitched together to cover the central area of the samples. Height maps were acquired for all sections through the laser scanning. A thresholding algorithm was applied with the purpose to quantify porosity, average pore radii, and wall thickness.

Tensile characterization

The micro-tensile characterization was performed by means of an micro-tensile developed in-house. The equipment featured a 5 N load (Honeywell Model, maximum error 0.1%) and a displacement actuator with a resolution of 50 nm.

Five samples of PUR scaffolds were obtained by cutting the original parallelepiped scaffold, pull out from the molds, with a cutting blade. Sample width was 2.0 mm, and sample length was greater than 7.5 mm to ensure a proper gripping region at the two ends of the samples; the distance between the gripped regions was 7.5 mm.

Displacement tests were performed at a 1 $\mu m\ s^{-1}$ loading rate until rupture of the sample occurred.

Microcompression characterization

Unidirectional quasi-confined compression tests were carried out on PUR scaffolds in dry and wet conditions at room temperature. Samples were cut taking care that the sample size was suitably larger than the probe size to avoid size or boundary effects. Sample thickness was about 7 mm, one order of magnitude larger than the maximum penetration depth. Stainless steel flat circular punches with a diameter of 2 mm were used. The wet conditions were obtained by soaking the sample in water for 24 h before testing and holding the samples in a liquid cell throughout the test. The displacement-controlled tests were performed by applying 20 incremental steps of 10 μm at a constant displacement rate (50 nm s^{-1}) with a holding phase of 10 s and partial unloading of 5 μm at 100 $\mu\ s^{-1}$ at each step; a maximum penetration depth of 2100 μm was achieved at the end of the test. At least five repetitions of the compression tests were performed on different locations of the scaffold. The unloading branches were used to estimate the slope of the force–displacement curve $S = dF/du$. The unloading slope was estimated through linear fitting of force–displacement data within 80% and 20% of the current maximum load. The reduced modulus was obtained as $E\_r = S/2R$, with R being the punch radius. Under the assumption of linearized isotropy, the reduced modulus is related to the Young's modulus and Poisson's ratio as $E\_r = E/(1-\nu\hat{}2)$. Since a comparison with the elastic modulus obtained through the tensile tests is of interest, the elastic modulus in compression was evaluated at the same equivalent strain ($\varepsilon \approx 10\%$); this was achieved by estimating S at a penetration depth u_c of approximately $u\_c = \varepsilon\_tH$, where H is an effective thickness here assumed to be $H = 2R$.

Contact angle measurements

Static contact angle measurements were carried out on scaffolds (three points for each sample) using a KSV CAM2000 (KSV Instruments LTD, Finland) system equipped with a liquid dispenser, video camera, Attension Theta software, and the sessile drop method in advancing mode. Distilled water drops of 5 μl were gently deposited onto five regions of the sample surfaces. Attension Theta software performed automated curve fitting of the drop profile based on the Young–Laplace equation.

Scanning electron microscopy (SEM)

SEM was performed using a LEO 1420 microscope (Zeiss, Germany) at 20 kV and a working distance of 15 mm. Longitudinal and cross sections were obtained by cutting the specimens after freezing in liquid nitrogen. Micrographs of these sections were recorded with magnifications of 150, 250, 1000, and 1500×.

Primary cardiomyocytes isolation and culture

The procedure of cardiomyocytes isolation was in agreement with the Guide for the Care and Use of Laboratory Animals published by the US National Institutes of Health, and was approved by the Animal Care and Use Committee of Turin University. Neonatal rat ventricular myocytes were isolated from 2 or 3-day-old Sprague–Dawley rat hearts by several rounds of digestion with collagenase type II (Worthington Biochemicals, Lakewood, NJ, USA) and pancreatine (Sigma-Aldrich, Italy) as previously described [28]. Briefly, hearts from neonatal rats were collected, atria excised, and the ventricles minced in Hank's Balanced Salt Solution buffer (116 mM NaCl, 20 mM HEPES, 1 mM NaH_2PO_4, 5.4 mM KCl, 5.5 mM glucose, 0.8 mM $MgSO_4$, pH 7.35) containing 432 $\mu g\,ml^{-1}$ collagenase type II and 666 $\mu g\,ml^{-1}$ pancreatine. Six rounds of digestion were performed at 37 °C for 10 min each. Fibroblasts were removed by two rounds of pre-plating for 1 h each on plastic TCPs. Cardiomyocytes were seeded on fibronectin-coated plastic TCPs (n = 6) and on PUR-PAA-fibronectin scaffolds (n = 6) placed in a 48-well plate and allowed to adhere for two days. Cardiomyocytes were maintained in Dulbecco's Modified Eagle Medium–M199 medium, 10% horse serum (Gibco, Italy), and 5% new calf serum (Gibco, Italy). During the third and fourth days of culture, cardiomyocytes were maintained in the presence of 1 $\mu g\,ml^{-1}$ of Ara-C to inhibit fibroblast proliferation.

Viability assay

CellTiter Blue was mixed with the cell culture medium at a concentration of 20% (v/v). At each time point, cardiac constructs cultured in 48-well plates were washed with phosphate buffered saline (pH 7.4) to remove the medium, and then 500 μl of the assay mixture was added to each sample. After 1 h, 100 μl was removed from the plates, and fluorescence was measured in a 96-well plate using a GloMax-Multi-detection System (Promega, Milan, Italy) at λ_{ex} = 525 nm and λ_{em} = 580–640 nm.

Analysis of scaffold colonization and beating activity

Immunofluorescence staining was performed on primary cultures to assess the percentage of cardiomyocytes and fibroblasts. F-actin was revealed with fluorescein isothiocyanate-labeled phalloidin (F432, Thermo Fisher Scientific, USA) diluted to 1:400; sarcomeric α-actinin was stained using the mouse monoclonal Ab (EA-53, ab9465, Abcam, UK) diluted to 1:50. Alexa Fluor 488 goat anti-mouse (Thermo Fisher Scientific, USA) and Alexa Fluor 546 goat anti-rabbit (Thermo Fisher Scientific, USA) were used as secondary antibodies. DAPI (4′,6-diamidino-2-phenylindole, Sigma-Aldrich, USA) at 1:1000 was added to highlight nuclei of each sample. For beating activity, cardiomyocytes were stained with CellTracker Orange (Invitrogen, Milan, Italy) following the manufacturer's instructions. Next, 1×10^6 cardiomyocytes were plated on each scaffold. Video microscopy acquisitions were performed using Zeiss Observer Z1 microscopy equipped with AxioVision 4.8 software.

Western blot

Hearts were lysed in Tris-buffered saline with 1% sodium dodecyl sulfate, containing Roche complete protease inhibitor cocktail, 10 mM NaF, 1 mM phenylmethylsulfonyl fluoride, and 1 mM Na_3VO_4. Protein extracts were prepared as previously described [29]. Western blot band quantifications were performed with Quantity One software (Bio-Rad Laboratories Inc., Hercules, CA, USA). For Western blot analysis antibodies against the following proteins were used: phospho-T202/Y204 ERK1/2 (Cell Signaling, Danvers, MA, USA), total ERK1 (Santa Cruz Biotechnology, Dallas, TX, USA), phospho-S473-AKT, and total AKT (Cell Signaling, Danvers, MA, USA). Western blot band quantifications were performed with Quantity One software (Bio-Rad Laboratories Inc., Hercules, CA, USA).

RNA extraction and reverse transcription for real-time quantitative polymerase chain reaction (PCR) analysis

After 14 days in culture, cardiomyocytes were recovered from the scaffolds and tissue culture dishes by repeated flushing with TRI Reagent (Sigma-Aldrich, Milan, Italy) on ice. Total RNA was extracted using the acid guanidinium thiocyanate-phenol-chloroform method by RNeasy Mini kit (Qiagen S.p.A, Italy, MI). The RNA concentration and purity were spectrophotometrically determined, and 1 μg of total RNA was reverse-transcribed in cDNA according to the manufacturer's protocol (Thermo Fisher Scientific, USA). Probes and primer pairs specific for all genes analyzed and for housekeeping genes were designed with specific software (Applied Biosystems Primer Express Version 2.0) and are reported in table 1. Reaction conditions of all primer pairs or probes were optimized, and real-time PCR analysis was performed in triplicate following accurate and standardized protocols.

Table 1. Designed primer/probe set for structural, apoptosis, glucose, and fatty acid metabolism, natriuretic peptides, and biological receptors, endothelin-1 genes, as well as housekeeping genes. TBP: TATA box binding protein; PPIA: peptidylprolyl isomerase A (cyclophilin A); RPL13a: ribosomal protein L13a; ACTC1: actin alpha cardiac muscle 1; MYH7: myosin heavy chain 7, cardiac muscle beta; MYH6: myosin heavy chain 6, cardiac muscle alpha; TNNI3: troponin I3, cardiac type; CTGF: connective tissue growth factor; BAX: BCL2-associated X, apoptosis regulator; BCL2: BCL2 apoptosis regulator; SLC2A1: solute carrier family 2 member 1; PFKL: phosphofructokinase, liver type; GCKR: glucokinase (hexokinase 4) regulator; PDK4: pyruvate dehydrogenase kinase, isozyme 4; PPAR-δ: peroxisome proliferator-activated receptor delta; PPAR-α: peroxisome proliferator-activated receptor alpha; PGC1-α: coactivator 1 alpha; ANP: atrial natriuretic peptide; BNP: B-type (or brain) natriuretic peptide; CNP: C-type natriuretic peptide; NPR-A: natriuretic peptide receptor A; NPR-B: natriuretic peptide receptor B; Prepro-ET-1: endothelin-1 gene.

Gene	GenBank, accession #	Amplicon length
TBP	NM_001004198	75 bp
PPIA	NM 017101	149 bp
RPL13A	NM_173340	66 bp
ACTC1	NM_019183.1	79 bp
MYH7	NM_017240.2	76 bp
MYH6	NM_017239.2	71 bp
TNNI3	NM_017144.2	59 bp
CTGF	NM_022266.2	59 bp
BAX	NM_017059.2	57 bp
BCL2	NM_016993.1	104 bp
SLC2A1	NM_138827.1	73 bp
PFKL	NM_013190.4	60 bp
GCKR	NM_013120.2	67 bp
PDK4	NM_053551.1	76 bp
PPAR-δ	NM_013141.2	94 bp
PPAR-α	NM_013196.1	98 bp
PGC1-α	NM_031347.1	94 bp
TBP	NM_001004198	123 bp
PPIA	NM 017101	135 bp
RPL13A	NM_173340	130 bp
ANP	NM_012612	118 bp
BNP	NM_031545	187 bp
CNP	NM_053750	201 bp
NPR-A	NM_012613	81 bp
NPR-B	NM_053838	89 bp
Prepro-ET-1	NM_012548	98 bp

Statistical data analysis

Differences between more than two independent groups were analyzed by Fisher's test after ANOVA or by Bonferroni's test when indicated. Results are expressed as mean $\pm$ SEM, and the p-value was considered significant when < 0.05. GeNorm software was used to define the most stably expressed gene set (TATA binding protein (TBP), peptidylprolyl isomerase A (PPIA), and ribosomal protein L13a (RPL13a); the geometric mean of the latter was used for normalization of real-time PCR results. Relative quantification of each target gene studied was calculated by the ΔCt method using Bio-Rad CFX96 manager software (CFX96 Real-Time PCR detection systems, Bio-Rad Laboratories Inc., Hercules, CA, USA). Differences between more than two independent groups were analyzed by Fisher's test after ANOVA using Statview 5.0.1 software released for Windows Statistical Analysis System (SAS Institute, Inc., Cary, NC, USA). The results are expressed as mean $\pm$ SEM, and the p-value was considered significant when < 0.05.

Results

Polyurethane characterization

PUR was successfully synthesized as confirmed by ATR-FTIR spectroscopy and SEC analysis. The formation of urethane linkages was evidenced by the appearance of two absorption bands, one at 1629 cm^{-1}, due to C=O stretching (amide I), and the other at 1535 cm^{-1} attributed to N–H bending vibrations (amide II). The urethane group also showed absorption at 3330 cm^{-1}, which was ascribed to N–H stretching. The strong absorption at 1725 cm^{-1} was attributed to the stretching of the carboxyl group in the macrodiol (PCL). Another strong peak was observed at 1160 cm^{-1} and was due to the stretching of the C–O–C linkage. The PUR number-average molecular weight (M_n) measured by SEC was 70.5 KDa, and the polydispersity index D (M_w/M_n) was 1.3.

Scaffold characterization

Morphological, tensile, and microcompression scaffold characterization

The morphological characterization of the porous scaffold performed though confocal laser microscopy showed an average porosity of 37 $\pm$ 3%. The average radius of the pores was similar for all samples: 37.2 $\pm$ 3.0 μm. The wall thicknesses were 10.7 $\pm$ 3.9 μm and 6.0 $\pm$ 1.5 μm (figure 1).

All measures presented a standard deviation within 10% with the exception of wall thickness, for which the standard deviation was up to 38%.

Under uniaxial tensile load, the PUR scaffold showed an elastic modulus in dry state in the order of 1 MPa, while the maximum stress achieved was 0.28 MPa.

The stress–strain curves showed a scattered response; however, the standard deviation estimated on the elastic modulus was within 25% of the average values. The unloading branches of microcompression tests were used to assess the elastic modulus upon compression. The elastic indentation moduli estimated under compression at approximately 10% of compression strain were 0.62 $\pm$ 0.16 MPa and 0.34 $\pm$ 0.19 MPa for dry and liquid environments, respectively. The difference in indentation moduli between dry and liquid conditions was statistically significant ($p < 0.05$). The elastic modulus of the sample tested in the wet environment was about 50% of that of the sample tested in the dry state; this behavior can

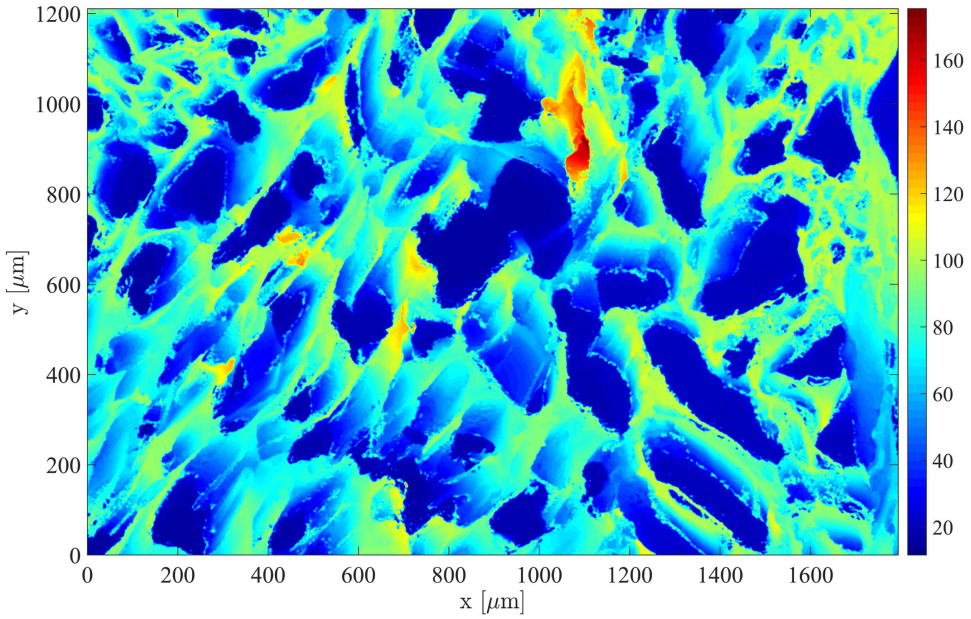

Figure 1. Transverse cross section of the PU scaffold; color scale refers to height measures obtained through the confocal laser scanning microscope.

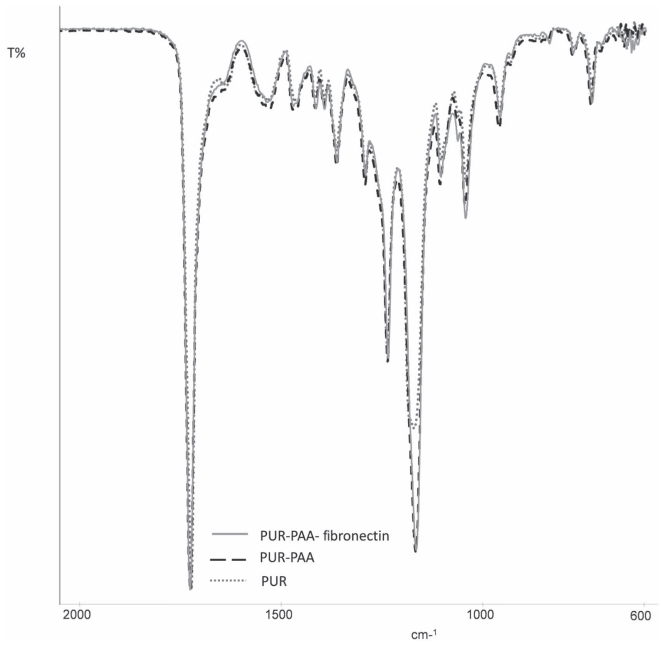

Figure 2. ATR-FTIR spectra of PUR, PUR-PAA, and PUR-PAA-fibronectin scaffolds.

be ascribed to the plasticizing effect of the aqueous environment [30].

The stiffness of myocardial tissue was evaluated in the range of 10–20 kPa at the beginning and 200–500 kPa at the end of diastole [12]. Hence, the properties found in this work are consistent with those of the myocardial tissue. It should be observed that similar scaffolds studied in a previous work [25] showed an elastic modulus under tension of 1.5 MPa and 0.3 MPa in dry and wet conditions, respectively. These values are consistent with those found in the present study.

ATR-FTIR studies

Figure 2 shows the ATR-FTIR spectra of PUR, PUR-PAA, and PU-PAA-fibronectin scaffolds in the range of 2000–900 cm^{-1}.

This range was selected to better elucidate the slight variation in the three spectra. The ATR-FTIR spectra of the PUR-PAA and PU-PAA-fibronectin

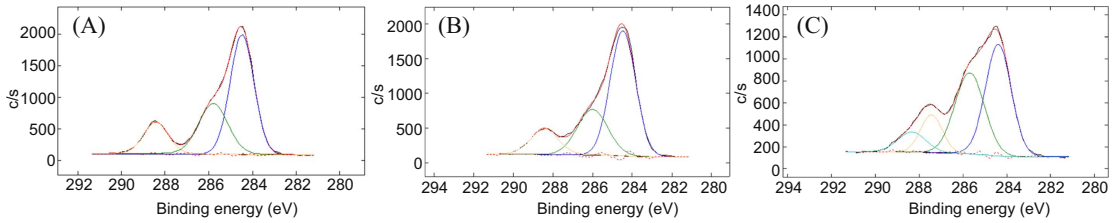

Figure 3. Deconvolution of XPS core level C1s spectra of (a) PUR, (b) PUR-PAA, and (c) PUR-PAA-fibronectin scaffolds.

Table 2. XPS atomic composition of PUR, PUR-PAA, and PUR-PAA-fibronectin scaffolds.

Sample	C (%)	O (%)	N (%)
PUR	71.6	21.6	5.4
PUR-PAA	67.0	27.5	2.4
PUR-PAA-fibronectin	63.4	22.0	11.8

Table 3. Relative intensity data of the deconvoluted C1s core level spectra of PUR, PUR-PAA, and PUR-PAA-fibronectin scaffolds.

	C			
Scaffolds	C–C, C–H	C–O, C–N	CONH	COOH, COOR
PUR	15.6	29.6	—	54.9
PUR-PAA	14.2	26.4	—	59.4
PUR-PAA-fibronectin	8.4	35.7	12.3	43.6

scaffolds showed characteristic absorptions of both polyurethane and polyacrylic polymers, indicating an average coating thickness below the one measured by this method (about 0.65 μm). The spectra of PUR-PAA and PUR-PAA-fibronectin scaffolds were very similar. The main differences between these spectra and that of the PUR scaffold can be observed in the region of the C=O stretching. The spectrum of the PUR scaffold showed a strong absorption at 1725 cm $^{-1}$, attributed to the ester group of the poly-urethane backbone, and a weak peak at 1629 cm^{-1} due to the urethane linkage. The spectra of PUR-PAA and PUR-PAA-fibronectin scaffolds showed the main peak and a broad shoulder at lower frequencies; this was due to signal overlapping of urethane, carboxyl, and amide groups. Moreover, compared to the PUR scaffold, the functionalized scaffolds showed a higher intensity of the C–O–C stretching peak (1160 cm^{-1}), which can be ascribed to the presence of carbonyl groups.

XPS

In table 2, the concentrations of the main elements present on the scaffold surfaces are summarized. These concentrations were obtained through XPS.

XPS analysis (figure 3) confirmed the surface immobiliza-tion of fibronectin by the observed changes in both chemical composition and C1s signal deconvolution shape of samples before and after the functionalization step. The O/C ratio showed the highest value on the PUR-PAA surface, which was due to the presence of a layer rich in carboxyl groups. However, the PUR-PAA surface had an oxygen composition lower than the theoretical value (27.5% instead of 40%) and an abnormal presence of nitrogen, probably due to two different reasons: (a) plasma-induced graft polymer-ization generated a cross-linked layer of poly(acrylic acid) instead of a linear polymeric chain, and (b) the PAA layer had a thickness that was below the XPS sampling depth, including the PUR substrate, as observed in our previous work [31].

The highest N/C ratio was observed in the PUR-PAA-fibronectin sample, which is in agreement with the presence of the protein. The deconvolution of the core level C1s peaks on pristine PUR and PUR-PAA surfaces (table 3) showed three contributions at 284.5, 286.0, and 288.5 eV, which may be assigned to the aliphatic C–H and C–C, to the C–O and C–N bond, and to the COOR and COOH groups, respectively.

The peak at 288.5 eV had higher values in virgin PUR and PUR-PAA surfaces, which was due to the presence of several ester groups in the macrodiol component of PUR and the carboxylic groups in the poly(acrylic acid) acid layer. The relative intensity of COOH–COOR groups in the PUR-PAA surface was 14.2%, lower than the theoretical value of pure PAA (close to 33%); this confirmed that the thickness of the PAA layer is less than the XPS sampling depth (a few nanometers). The PUR-PAA-fibronectin sample showed an additional peak at 287.4 eV, which can be assigned to the amide carbon. Compared to PUR and PUR-PAA scaffolds, the PUR-PAA-fibronectin sample exhibited a higher percentage of C bonded to N and O, and lower percentages of C bonded to C and H of ester and carboxylic groups; this was due to the pro-tein chemical composition. However the atomic com-position differed from the theoretical one calculated from the amino acid composition of fibronectin, as provided by the fibronectin supplier (data reported in the supplementary information file is available online at stacks.iop.org/BMM/13/055006/mmedia). For instance, the XPS analysis of PUU-PAA-fibronectin exhibited an amount of N lower than the theoretical value of pure fibronectin (11.8% versus 17.59%) and a quantity of O higher than the theoretical one (22%versus 18.90%), thus indicating that the underlying

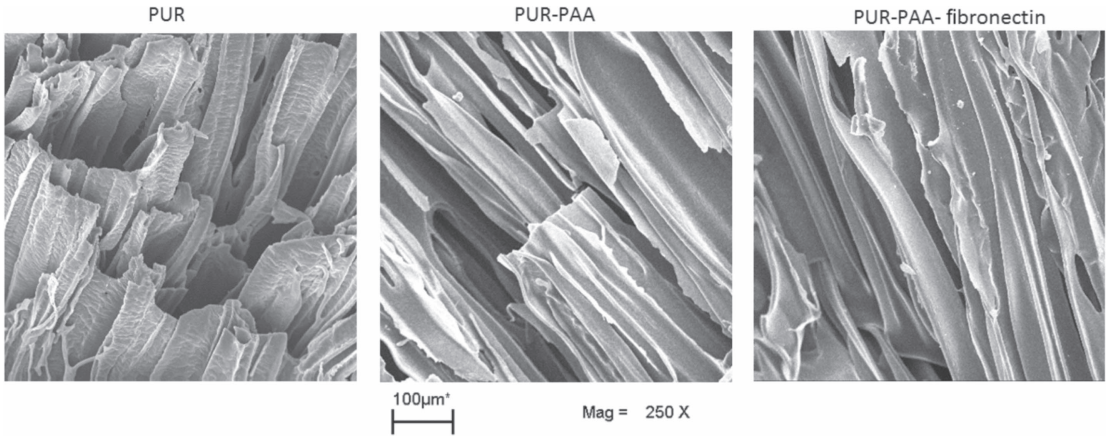

Figure 4. Micrographs of (a) PUR scaffolds, (b) PUR-PAA scaffolds, and (c) PUR-PAA-fibronectin scaffolds.

Table 4. Scaffold contact angle results.

Scaffold	Angle (°)
PUR	113.3 ± 3.7
PUR-PAA	113.0 ± 3.3
PUR-PAA-fibronectin	109.8 ± 2.5

PUU-PAA layer is partly detected. This leads to the assumption that the fibronectin layer is thinner than the XPS sampling depth. Similar observations were reported in a former publication [31]. In conclusion, XPS analysis (figure 3) confirmed the success of fibronectin immobilization in a layer with a few nanometer thickness.

Contact angle

Table 4 summarizes the water contact angle measurements. The water contact angle values on PUR and PUR-PAA scaffolds were around 113°, indicating that the surfaces were hydrophobic.

The corresponding value for the PUR film is around 79.3°. The higher hydrophobicity of scaffolds compared to the film can be explained by the different surface morphologies and roughness [32]: the scaffold has an aligned fiber-like structure, as evidenced by the SEM micrographs described below, and this is expec-ted to strongly affect the hydrophobicity of samples [33]. No significant differences can be observed after fibronectin immobilization; this result is in agreement with the hydrophobic nature of fibronectin surfaces [34].

SEM

Figure 4 shows the micrographs of PUR scaffolds, PUR-PAA scaffolds, and PUR-PAA-fibronectin scaffolds.

The figure shows an oriented parallel pore structure resembling the histoarchitecture of the myocardium. PUR-PAA and PUR-PAA-fibronectin micrographs show the pores' inner morphologies, which exhibit a lamellar substructure. A similar morphology was observed by Guan and colleagues [35].

Characterization of primary cardiomyocyte population

Once structurally and mechanically characterized, the capacity of scaffolds to support primary cardiomyocytes was assessed. This is described in the subsection 'Primary cardiomyocytes isolation and culture'. Immunofluores-cence analysis with an anti-sarcomeric actinin antibody and phalloidin was performed to characterize the cell population and to determine the ratio of myocyte to non-myocyte cells. Our analysis demonstrated that the percentage of cardiomyocytes was higher than 80%during the 14 days of experiment (figure 5).

Cardiomyocytes colonization and survival on the PUR-PAA-fibronectin scaffold

Primary cells colonized the scaffold surface and remained adherent to it for more than 50 days (figure 6(a)). Furthermore, the histological analysis with haematoxylin and eosin staining, performed on constructs after 14 days of culture, showed the presence of multiple cell layers on the scaffold surface (white arrows in figure 6(b)). Moreover, cell viability remained high and stable until day 14 (figure 6(c)).

Cardiomyocytes beating activity

Video microscopy acquisition demonstrated that cardiomyocytes seeded on the scaffolds beat synchronously for over 50 days (see supplementary material movie S1). These results demonstrated that cardiomyocytes survived and showed an intense beating activity on scaffolds.

Signal transduction activity of cardiac constructs As shown in figure 7, the activation of two important signaling pathways, the PI3K/AKT and MAPK pathways, was analyzed. Results demonstrated that the phosphorylation of AKT and ERK1/2 was higher in

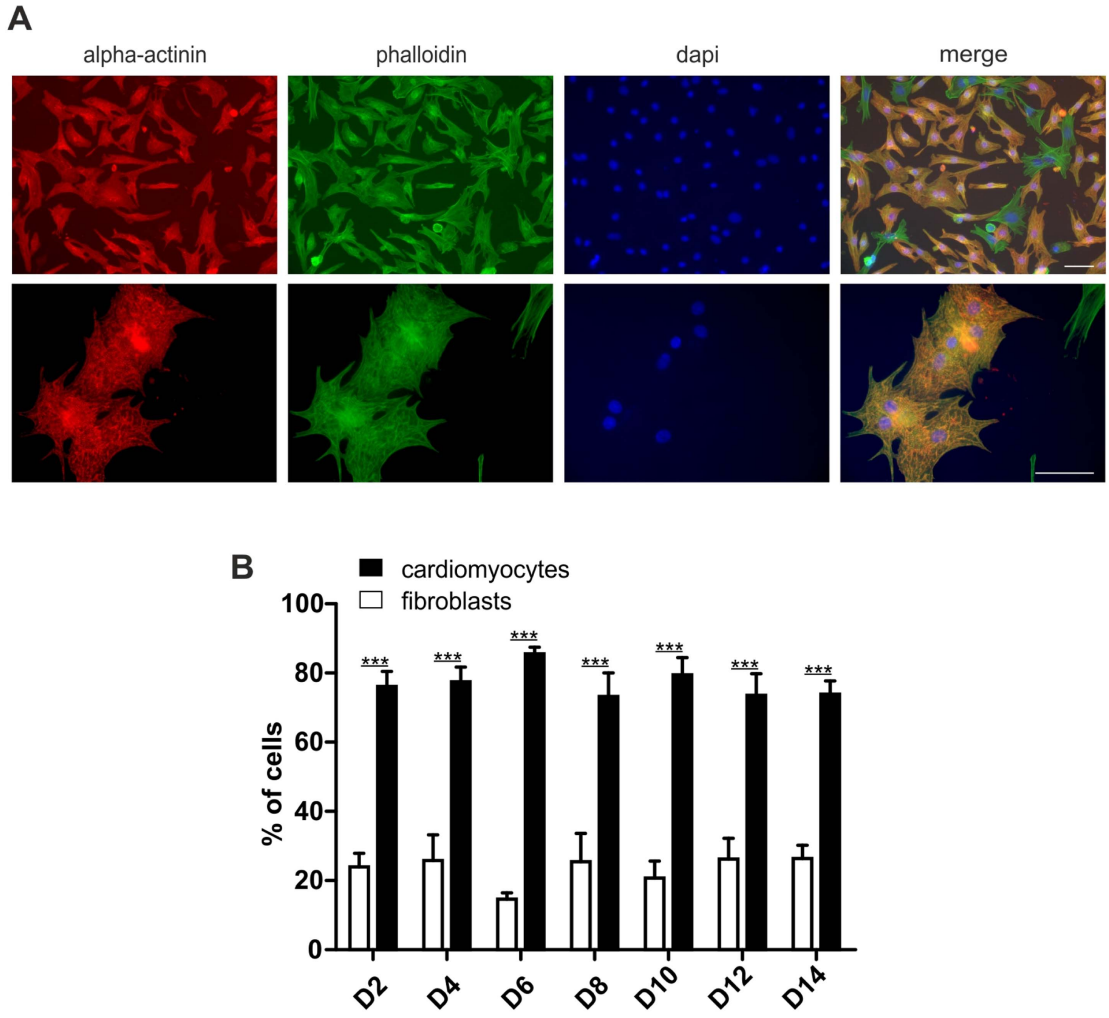

Figure 5. Characterization of primary cardiomyocytes population. Purity of primary neonatal heart cell culture. (a) Primary neonatal heart cells were subjected to immunofluorescence analysis using anti-sarcomeric α-actinin (red) and phalloidin (green) staining to evaluate the percentage of cardiomyocytes. Cells positive for sarcomeric α-actinin, were identified as cardiomyocytes. The pictures refer to cells stained four days after isolation. Cell nuclei were counterstained with DAPI (blue) (bars = 50 μm). (b) The percentage of cardiomyocytes present in the culture from day 2 (D2) to day 14 (D14). No significant difference was found across the percentages of cardiomyocytes or fibroblasts at the different time points ($p > 0.05$). Instead, significant differences ($^{***}p < 0.001$) were found between fibroblasts and cardiomyocytes at each time point. Statistical analysis was performed using one-way ANOVA followed by Bonferroni post test.

cardiomyocytes cultured on the scaffold compared to those cultured on plastic plates.

Gene expression profiling

The global mRNA expression changes between TCP and scaffold groups of natriuretic peptides (ANP, BNP, and CNP) together with their specific guanylate cyclase receptors (NPR-A and NPR-B) and endothelin-1 (prepro-ET-1) are reported in figures 8 and 9.

No statistical differences were observed for the expression of the three natriuretic peptides in TCP compared with scaffolds (figures 9(a)–(c)). Meanwhile, natriuretic peptides (NP) receptors were counter-regulated with respect to their related biological ligands, significantly only for NPR-A expression ($p = 0.018$) (figure 8(a)). In the same samples, a statis-tical significance was observed for prepro-ET-1 mRNA expression (figure 8(b)), which was higher ($p = 0.035$) after 14 days of culture on the scaffold surface.

Cardiac muscle- and hypertrophy-specific genes, involved in heart development and function were modulated between cell grown for 14 days on scaffolds and on TCPs. In particular, MYH7 was significantly upregulated on scaffolds compared to plates (figure 8(c)). ACTC1 (figure 10(a)) and apoptotic genes (i.e. BAX, BCL2) did not show any statistically significant difference (figure 10(b)).

The hypertrophy-related gene (CTGF) was upregulated on TCPs at 14 days compared to scaffolds (figure 8(d)). Metabolic-specific genes were differentially regulated between cells grown on scaffolds and on plates. Glucose metabolism showed a statistically significant upregulation (SLC2a1 and PFKL genes in figures 8(e) and (f), respectively) in cells on scaffolds compared to TCPs. Conversely, fatty acid oxidation was not significantly modulated (PGC1-α, PPAR-α,

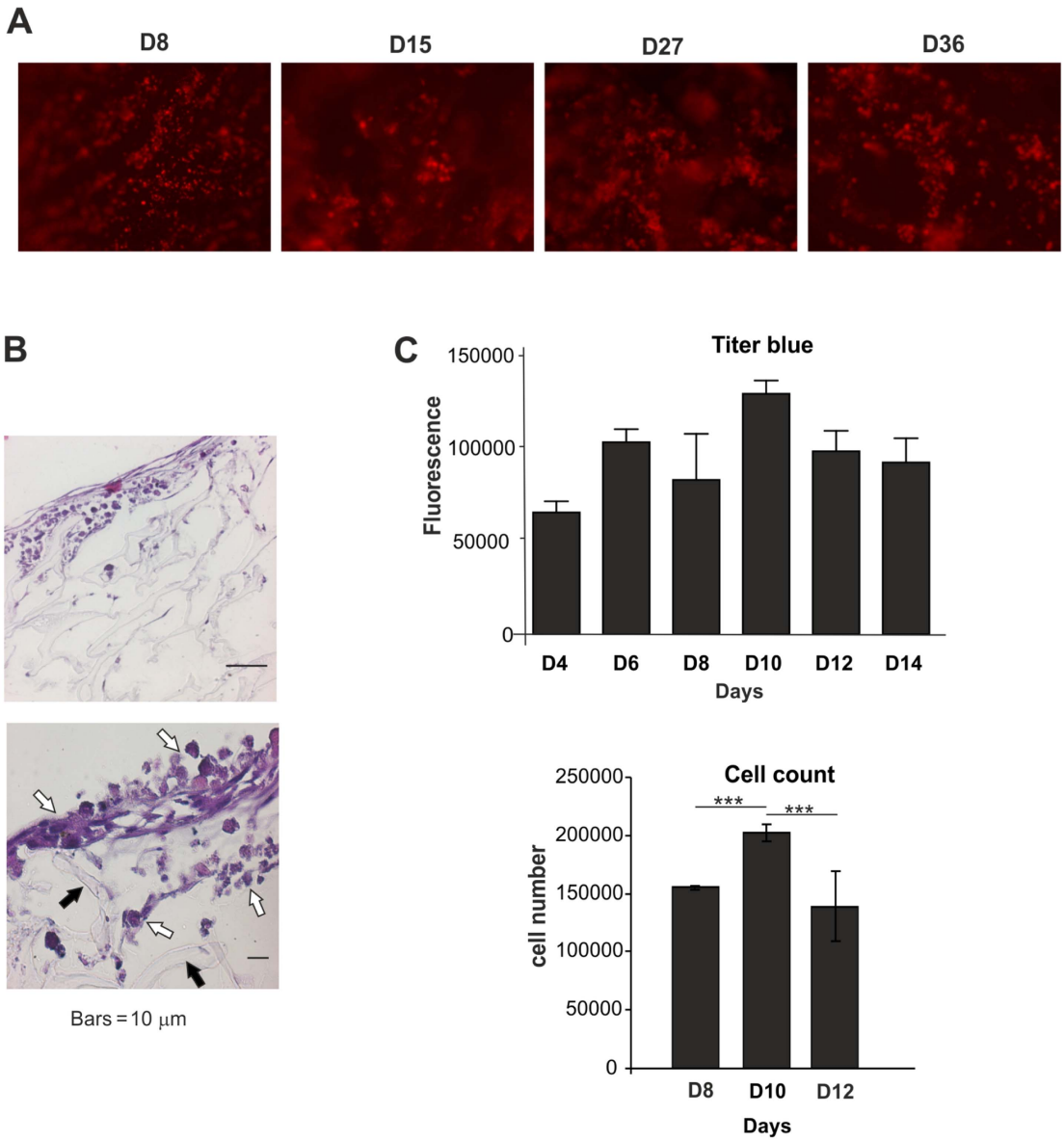

Figure 6. Adhesion and viability of cardiomyocytes on the scaffold. (a) Primary cells were stained with Acridine orange and then seeded on the scaffolds and allowed to adhere for two days. From four days after cell seeding, constructs were analyzed using fluorescence microscopy to evaluate the scaffold colonization. (b) Serial sections from cardiac constructs after two weeks of culture were obtained and stained with haematoxylin and eosin. White arrows indicate cardiomyocytes, while black arrows mark scaffold fibers (bars $= 10\ \mu$m). (c) Results of CellTiter Blue assay performed from day 4 (D4) to day 12 (D12) on the cardiac constructs ($n = 3$). Differences were not statistically significant. Cell count analyses from day 8 to day 12 (D8–D12) were also performed on cardiomyocytes cultured on the scaffolds. Significant differences ($^{***}p < 0.001$) were found using one-way ANOVA followed by Bonferroni post test.

and PPAR-δ genes in figures 10(c)–(e), respectively) in cells grown on scaffolds compared to TCPs.

Discussion

The development of efficient cardiac models is a challenge in tissue engineering because of the muscle's particular characteristics; furthermore, the tissues are continuously subjected to several stimuli (neural and hormonal signals, ion currents, changes in preload and afterload) and able to modify their cellular responses. The use of classic two-dimensional cell cultures of rat cardiomyocytes has greatly advanced cardiac cell function knowledge [36]. However, the lack of their tissue-level organization characterized by cell interactions with the ECM and mechanical forces, which are important to maintain cell morphology, maturity, and function [37, 38], have led to researchers reproducing the 3D environment. In fact, 3D engineered tissues have been demonstrated to (i) induce or recreate pathological situations, (ii) provide measurable indicators to monitor damaging or healing processes, (iii) supply accurate evaluation of drug safety, and, therefore, eliminate toxic and ineffective compounds at an earlier stage, and (iv) reproduce the

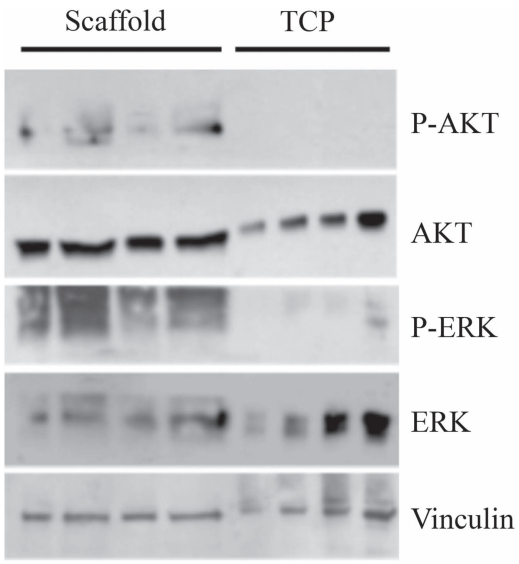

Figure 7. Signal transduction activity of cardiac constructs. Western blot analysis of P-ERK, total ERK, P-AKT, and total AKT on primary cells grown on scaffolds or on TCP for 14 days. The graph shows densitometry quantification of western blot bands ($n = 5$)

ECM properties at different aging levels to better understand the effects of age and/or pathological conditions on tissue properties and functionality [39].

The tissue engineering approach used in this work allowed us to build an *in vitro* model able to recapitulate various physiological functions of the myocardial tissue. The present PUR-based 3D *in vitro* model was characterized to ensure the replication of the cardiac structure from the morpho-mechanical and biological point of view: the first goal was obtained by mimicking the tissue-specific architecture and mechanical properties [3, 4], and the second goal was realized by the use of appropriate cell types (primary cardiomyocytes) and the integration of ECM proteins.

Tensile tests showed that the scaffold elastic modulus in the dry state is about 1 MPa, while the compression elastic moduli in dry and wet conditions were 620 KPa and 340 KPa, respectively. These mechanical properties are consistent with those of the myocardial tissue [12].

ATR-FTIR, contact angle, and XPS analysis confirmed the formation of a nanometric fibronectin layer after plasma treatment. This result is important since the low thickness of the modified surface is crucial to avoid affecting the scaffold mechanical properties, such as elastic modulus, tensile strength, and % elongation-to-break.

Finally, the scaffold microstructure was analyzed. SEM images showed an aligned pore structure, and confocal images revealed the average diameter and porosity (around 75 μm and 37%, respectively) to be similar to those of the heart. The pore size and porosity percentage are appropriate [16], and once the scaffold is implanted *in situ*, it is expected to promote the regeneration of blood vessels [40, 41] as well as fibroblast proliferation. These are crucial steps for the regeneration of a cardiac-like tissue [42].

The functionalized scaffold proposed as a myocardial model is highly hydrophobic, as shown by contact angle measurements. Several studies report that hydrophilic surfaces are suitable for cell attachment [43]. However, these observations are only valid in cases of flat or relatively smooth surfaces; in the case of porous scaffolds the correlation between hydrophilicity and cell adhesion is more complex. Several publications demonstrate that substrates from a hydrophobic material showing submicron roughness turn out to be highly hydrophobic [44, 45]. The high hydrophobicity of the proposed scaffolds can then be attributed to their fiber-like structure, but this surface property does not negatively affect cell adhesion.

The biological characterization of PUR-PAA-fibronectin scaffolds was carried out using primary cardiomyocytes from rat neonatal hearts as a reference system. Cardiomyocytes showed good surface colonization, as well as high and stable viability, which is comparable to the results observed by Rockwood [46]. Notably, cardiomyocyte beating activity was still present after seven weeks of culture, while cardiomyocytes cultured on TCPs did not survive more than three weeks.

Signal transduction is crucial for cardiomyocytes to sense mechanical stretch as well as humoral stimuli leading to hypertrophic growth, cardiomyocyte survival, and metabolic adaptation. In particular, our focus was directed at two main pathways: PI3K/AKT and MAPK. Their activation protects cardiomyocytes from damage and apoptosis induced by myocardial infarction [47–49], pressure overload [50], hypoxia [51], or hypoglycemia [52]. Notably, AKT and ERK1/2 phosphorylation in cardiomyocytes cultured on scaffolds was higher than in cells cultured on culture plates, thus providing a molecular explanation for the increased survival and functionality of cardiomyocytes cultured on scaffolds.

Biological characterization of scaffolds also involved the analysis of cell behavior correlated to important cardiac endogenous mediators, the cardiac natriuretic peptides. These are constituted by a family of peptide hormones and neurotransmitters, including ANP, BNP, and CNP. NPs play a role during physiological growth of the heart, and, mainly ANP/BNP, are able to stimulate proliferation and differentiation of fetal cardiomyocytes into mature ones [53, 54]. In this study, NPs were monitored to evaluate the potential maturation phenotype of cardiomyocytes. A trend in ANP reduction and an increase in both BNP and CNP expression in scaffolds was observed; this is in line with the fetal action of NPs and their guanylate cyclase-linked receptors NPR-A and NPR-B, which are known to be functionally redundant during early cardiovascular development [55]. In this paper, a different behavior of the three cardiac natriuretic

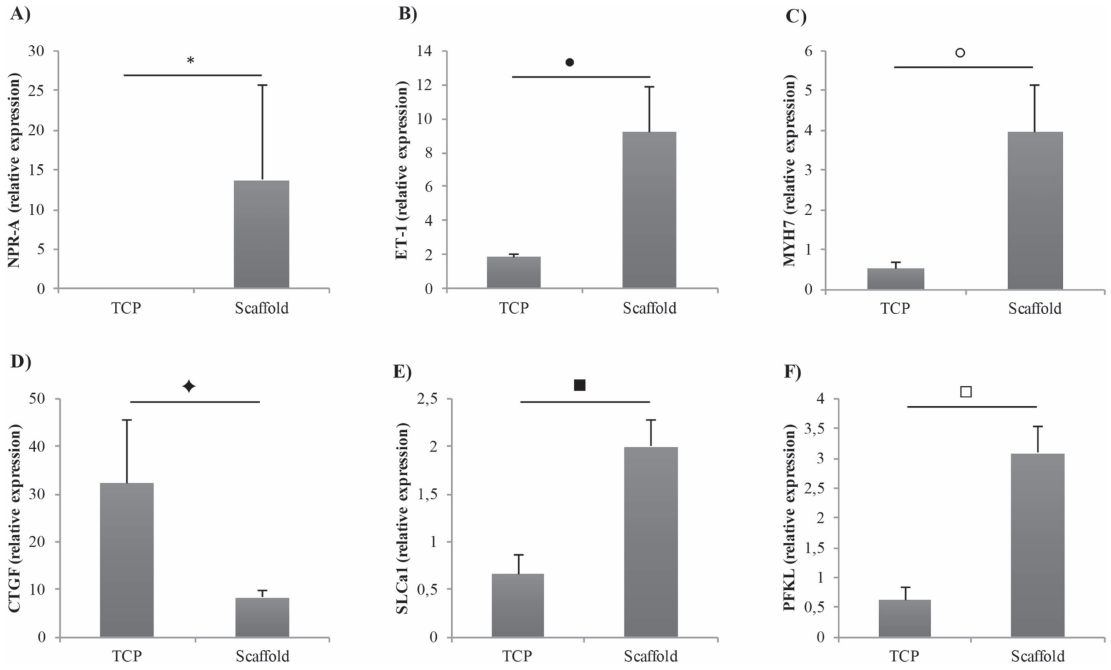

Figure 8. Analysis of significant modulation in cardiomyocyte gene expression. Expression of (a) NPR-A and (b) prepro-ET-1; (c, d) heart development and differentiation; and (e, f) heart glucose genes in cardiomyocytes grown on scaffolds and on TCP for 14 days. Results are the mean ± SEM. $^{*}p = 0.018$, $^{\bullet}p = 0.035$, $^{\circ}p < 0.05$, $^{\blacklozenge}p < 0.01$, $^{\blacksquare}p < 0.001$, $^{\square}p < 0.001$.

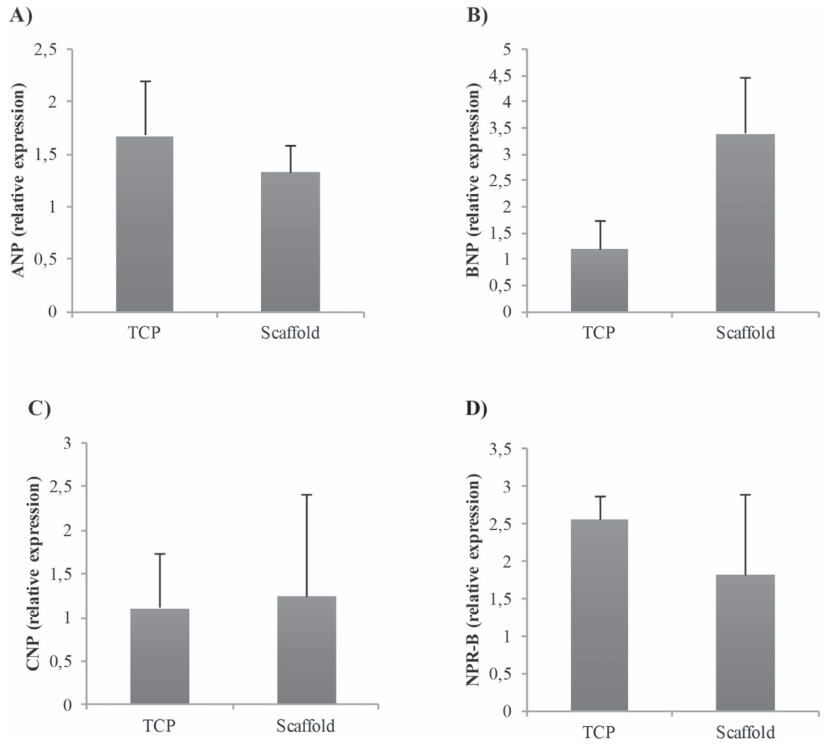

Figure 9. Analysis of cardiomyocyte gene expression. Expression of NP system genes in cardiomyocytes grown on scaffolds and on TCP for 14 days. Results are the mean ± SEM. No statistical significance was found ($p > 0.05$).

peptides in modulating cardiomyocyte proliferation by a counter-balancing of the two NP receptors (NPR-A and NPR-B) was observed. In fact, they increased (NPR-A) or decreased (NPR-B) in cardiomyocytes seeded on scaffolds compared to TCPs, thus confirming their down regulation with respect to their biological ligands (BNP and CNP, respectively). Moreover, for the first time a modulation of CNP, whose

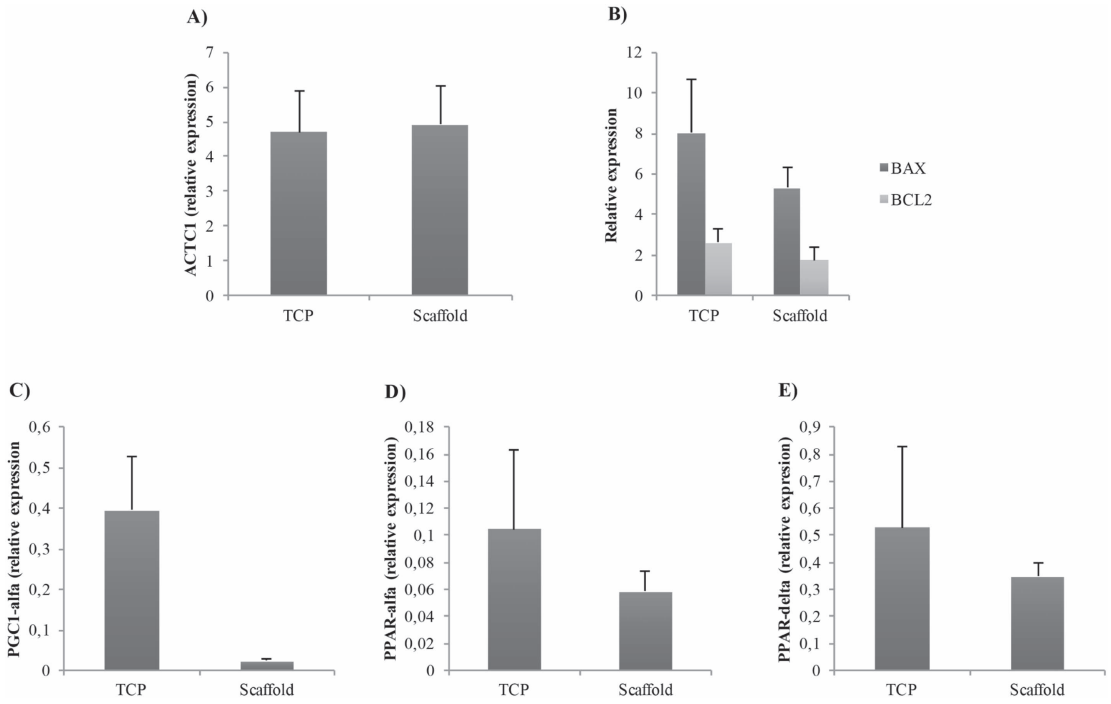

Figure 10. Analysis of cardiomyocyte gene expression: heart development, differentiation and apoptosis genes, fatty acid metabolism genes. Expression of (a) heart development and differentiation genes, (b) apoptosis genes, and (c–e) fatty acid metabolism genes in cardiomyocytes grown on scaffolds and on TCP for 14 days. Results are the mean ± SEM. No statistical significance was found.

expression reflects that of BNP, was observed, therefore underlining that during cardiomyocyte maturation NPs are modified in a different manner. These results are in line with a previous study where it was hypothesized that their trend during phenotype differ-entiation is probably caused by differences in sequence genes, rate of transcription, and differential stabiliza-tion of the mRNA [56].

Analysis of cell response to scaffolds involved also the evaluation of prepro-ET-1, a peptide secreted by many cell types (endothelial and epithelial cells, macrophages, fibroblasts) [57, 58] with potent vasoconstrictor and growth factor activity for a variety of cells, including cardiomyocytes [59, 60]. Prepro-ET-1 is involved in regulating cell cycle, and in cardiomyocytes induces a premature cardiomyocyte transition in the developing heart [57]. Our results suggested that prepro-ET-1 could promote a premature transition of fetal cardiomyocytes to a more mature phenotype.

A further biological characterization of the cardiomyocytes that colonized scaffolds was performed, analyzing specific apoptotic, cardiac muscle, hypertrophy- and metabolism-related genes. A non-significant modulation of apoptosis-related genes (BAX, BCL2) was observed between scaffolds and TCPs, showing a cell behavior that is in line with data from the literature [61, 62]. Cardiac muscle (MYH7) and hypertrophy-specific (CTGF) genes were, on the other hand, significantly modulated in scaffolds, in accordance with normal cardiac development and function [63–66], thus confirming an incipient process of cardiomyocyte maturation. Interestingly, glucose metabolism genes (SLC2a1, PFKL) were upregulated on scaffolds compared to plates while no statistically significant differences could be observed for fatty acid meta- bolism genes (PGC1-α, PPAR-α, and PPAR-δ). After 14 days on scaffolds, the absence of upregulation of fatty acid oxidation-related genes suggested a permanence of the myocardial cells in a fetal-like phenotype, still relying on glycolytic metabolism for their energy demand, and a delayed differentiation toward the adult phenotype [67, 68] that is instead characterized by a switch to the fatty acid β-oxidation route as a major source of energy [69]. Hence, the maintenance of high glycolytic rates in our developing cardiomyocytes grown on scaffolds seems to reflect cellular wellness, as they indeed maintain a good survival and proliferative state as previously observed [70–72].

Conclusion

In this work the feasibility of functionalized PUR-based scaffolds as a cardiac tissue model has been demon-strated, with a particular focus on the structural and mechanical mimicry offered by the biomaterial and on the biological behavior showed by seeded cells. In fact, success of plasma treatment to graft fibronectin on PUR scaffolds was observed via XPS analysis. Structural analysis showed a pore-aligned scaffold configuration, with mechanical properties and histoarchitecture resembling the myocardium. The biological characterization highlighted a stable viability for 14 days of experimentation, including good beating activity and

cell adhesion of cardiomyocytes. The increased levels of phosphorylation of AKT and ERK1/2 explained the prolonged cell survival and consequential beating activity of cardiomyocytes cultured on scaffolds versus TCPs. The modulation of cardiac muscle (prepro-ET-1, MYH7, CTGF) and glucose metabolism (SLC2a1, PFKL) genes indicates a transition phase in cardiomyocyte maturation, with an initial evolution to an adult phenotype as indicated by the former, and a permanence of some fetal characteristics shown by the sustained expression of the latter. These results represent the initial step to develop a new generation of tissue model systems with tunable structural and mechanical characteristics that are able to reproduce basic functional parameters of the entire heart, and to study cardiac physiology and pathophysiological mechanisms.

Acknowledgments

The authors declare no conflicts of interest. This study was funded by 'Engineering physiologically and pathologically relevant organ Models for the INvestigation of age related Diseases (MIND)' Project, PRIN 2010–2011 of Ministry of Education, University and Research (grant agreement 2010J8RYS7). This work is dedicated to Prof. Guido Tarone, brilliant scientist and dear colleague. Alessandra Piccitto and Giulia Quagliato are acknowledged for their support in sample preparation and characterization, respectively.

ORCID iDs

Federico Vozzi https://orcid.org/0000-0001-5457-2328

References

[1] Mendis S, Davis S and Norrving B 2015 Organizational update: the World Health Organization global status report on noncommunicable diseases 2014; one more landmark step in the combat against stroke and vascular disease *Stroke* **46** e121–2

[2] Mozaffarian D *et al* 2015 Heart disease and stroke statistics—2015 update: a report from the American Heart Association *Circulation* **131** e29–322

[3] Engler A J, Carag-Krieger C, Johnson C P, Raab M, Tang H-Y, Speicher D W, Sanger J W, Sanger J M and Discher D E 2008 Embryonic cardiomyocytes beat best on a matrix with heart-like elasticity: scar-like rigidity inhibits beating *J. Cell Sci.* **121** 3794–802

[4] Jacot J G, McCulloch A D and Omens J H 2008 Substrate stiffness affects the functional maturation of neonatal rat ventricular myocytes *Biophys. J.* **95** 3479–87

[5] Wobma H and Vunjak-Novakovic G 2016 Tissue engineering and regenerative medicine 2015: a year in review *Tissue Eng., Part B* **22** 101–13

[6] Shimizu T, Yamato M, Isoi Y, Akutsu T, Setomaru T, Abe K, Kikuchi A, Umezu M and Okano T 2002 Fabrication of pulsatile cardiac tissue grafts using a novel 3-dimensional cell sheet manipulation technique and temperature-responsive cell culture surfaces *Circ. Res.* **90** e40

[7] Kelm J M, Ehler E, Nielsen L K, Schlatter S, Perriard J-C and Fussenegger M 2004 Design of artificial myocardial microtissues *Tissue Eng.* **10** 201–14

[8] Kelm J M, Diaz Sanchez-Bustamante C, Ehler E, Hoerstrup S P, Djonov V, Ittner L and Fussenegger M 2005 VEGF profiling and angiogenesis in human microtissues J. *Biotechnol.* **118** 213–29

[9] Caddeo S, Boffito M and Sartori S 2017 Tissue engineering approaches in the design of healthy and pathological *in vitro* tissue models *Front. Bioeng. Biotechnol.* **5** 40

[10] Cooper S L and Guan J 2016 *Advances in Polyurethane Biomaterials* (Amsterdam: Woodhead Publishing)

[11] Carrier R L, Papadaki M, Rupnick M, Schoen F J, Bursac N, Langer R, Freed L E and Vunjak-Novakovic G 1999 Cardiac tissue engineering: cell seeding, cultivation parameters, and tissue construct characterization *Biotechnol. Bioeng.* **64** 580–9

[12] Chen Q-Z, Harding S E, Ali N N, Lyon A R and Boccaccini A R 2008 Biomaterials in cardiac tissue engineering: Ten years of research survey *Mater. Sci. Eng. R. Rep.* **59** 1–37

[13] Hidalgo-Bastida L A, Barry J J A, Everitt N M, Rose F R A J, Buttery L D, Hall I P, Claycomb W C and Shakesheff K M 2007 Cell adhesion and mechanical properties of a flexible scaffold for cardiac tissue engineering *Acta Biomaterialia* **3** 457–62

[14] Silvestri A, Boffito M, Sartori S and Ciardelli G 2013 Biomimetic materials and scaffolds for myocardial tissue regeneration *Macromol. Biosci.* **13** 984–1019

[15] Davis M E, Hsieh P C H, Grodzinsky A J and Lee R T 2005 Custom design of the cardiac microenvironment with biomaterials *Circ. Res.* **97** 8–15

[16] Boffito M, Sartori S and Ciardelli G 2013 Polymeric scaffolds for cardiac tissue engineering: requirements and fabrication technologies *Polym. Int.* **63** 2–11

[17] de Mulder E L W, Buma P and Hannink G 2009 Anisotropic porous biodegradable scaffolds for musculoskeletal tissue engineering *Materials* **2** 1674–96

[18] Kowligi R R, Maltzahn Von W W and Eberhart R C 1988 Fabrication and characterization of small-diameter vascular prostheses *J. Biomed. Mater. Res.* A **22** 245–56

[19] Thomas S P, Bircher-Lehmann L, Thomas S A, Zhuang J, Saffitz J E and Kleber A G 2000 Synthetic strands of neonatal mouse cardiac myocytes: structural and electrophysiological properties *Circ. Res.* **87** 467–73

[20] Pong T, Adams W J, Bray M-A, Feinberg A W, Sheehy S P, Werdich A A and Parker K K 2011 Hierarchical architecture influences calcium dynamics in engineered cardiac muscle *Exp. Biol. Med. (Maywood)* **236** 366–73

[21] Azarin S M, Lian X, Larson E A, Popelka H M, de Pablo J J and Palecek S P 2012 Modulation of Wnt/β-catenin signaling in human embryonic stem cells using a 3D microwell array *Biomaterials* **33** 2041–9

[22] To W S and Midwood K S 2011 Plasma and cellular fibronectin: distinct and independent functions during tissue repair *Fibrog. Tissue Repair* **4** 21

[23] Brancaccio M, Cabodi S, Belkin A M, Collo G, Koteliansky V E, Tomatis D, Altruda F, Silengo L and Tarone G 1998 Differential onset of expression of alpha 7 and beta 1D integrins during mouse heart and skeletal muscle development *Cell Adhes. Commun.* **5** 193–205

[24] Sartori S, Boffito M, Serafini P, Caporale A, Silvestri A, Bernardi E, Sassi M P, Boccafoschi F and Ciardelli G 2013 Synthesis and structure–property relationship of polyester-urethanes and their evaluation for the regeneration of contractile tissues *React. Funct. Polym.* **73** 1366–76

[25] Boffito M, Bernardi E, Sartori S, Ciardelli G and Sassi M P 2015 A mechanical characterization of polymer scaffolds and films at the macroscale and nanoscale *J. Biomed. Mater. Res.* A **103** 162–9

[26] Shahidi S, Wiener J and Ghoranneviss M 2013 Surface modification methods for improving the dyeability of textile fabrics *Eco-Friendly Textile Dyeing and Finishing* (Rijeka: InTech)

[27] Soonpaa M H and Field L J 1998 Survey of studies examining mammalian cardiomyocyte DNA synthesis *Circ. Res.* **83** 15–26

[28] De Acetis M *et al* 2005 Cardiac overexpression of melusin protects from dilated cardiomyopathy due to long-standing pressure overload *Circ. Res.* **96** 1087–94

[29] Sbroggiò M, Bertero A, Velasco S, Fusella F, De Blasio E, Bahou W F, Silengo L, Turco E, Brancaccio M and Tarone G 2011 ERK1/2 activation in heart is controlled by melusin, focal adhesion kinase and the scaffold protein IQGAP1 *J. Cell Sci.* **124** 3515–24
[30] Pan Z and Ding J 2012 Poly(lactide-co-glycolide) porous scaffolds for tissue engineering and regenerative medicine *Interface Focus* **2** 366–77
[31] Sartori S, Rechichi A, Vozzi G, D'acunto M, Heine E, Giusti P and Ciardelli G 2008 Surface modification of a synthetic polyurethane by plasma glow discharge: preparation and characterization of bioactive monolayers *React. Funct. Polym.* **68** 809–21
[32] Ballester-Beltrán J, Rico P, Moratal D, Song W, Mano J F and Salmerón-Sánchez M 2011 Role of superhydrophobicity in the biological activity of fibronectin at the cell–material interface *Soft Matter* **7** 10803–11
[33] Areias A C, Ribeiro C, Sencadas V, García-Giralt N, Diez-Perez A, Gómez Ribelles J L and Lanceros-Méndez S 2012 Influence of crystallinity and fiber orientation on hydrophobicity and biological response of poly(l-lactide) electrospun mats *Soft Matter* **8** 5818–25
[34] Hayashi-Nagai A, Kitagaki-Ogawa H, Matsumoto I, Hayashi M and Seno N 1991 Hydrophobic properties of porcine fibronectin and its functional domains *J. Biochem.* **109** 83–8
[35] Guan J, Fujimoto K L and Wagner W R 2008 Elastase-sensitive elastomeric scaffolds with variable anisotropy for soft tissue engineering *Pharm. Res.* **25** 2400–12
[36] Louch W E, Sheehan K A and Wolska B M 2011 Methods in cardiomyocyte isolation, culture, and gene transfer *J. Mol. Cellular Cardiol.* **51** 288–98
[37] Akins R E, Rockwood D, Robinson K G, Sandusky D, Rabolt J and Pizarro C 2010 Three-dimensional culture alters primary cardiac cell phenotype *Tissue Eng.* A **16** 629–41
[38] Kira Y, Nakaoka T, Hashimoto E, Okabe F, Asano S and Sekine I 1994 Effect of long-term cyclic mechanical load on protein synthesis and morphological changes in cultured myocardial cells from neonatal rat *Cardiovasc. Drugs Ther.* **8** 251–62
[39] Vacanti J 2010 Tissue engineering and regenerative medicine: from first principles to state of the art *J. Pediatr. Surg.* **45** 291–4
[40] Oliviero O, Ventre M and Netti P A 2012 Functional porous hydrogels to study angiogenesis under the effect of controlled release of vascular endothelial growth factor *Acta Biomaterialia* **8** 3294–301
[41] Madden L R, Mortisen D J, Sussman E M, Dupras S K, Fugate J A, Cuy J L, Hauch K D, Laflamme M A, Murry C E and Ratner B D 2010 Proangiogenic scaffolds as functional templates for cardiac tissue engineering *Proc. Natl. Acad. Sci. USA* **107** 15211–6
[42] Rnjak-Kovacina J, Wise S G, Li Z, Maitz P K M, Young C J, Wang Y and Weiss A S 2011 Tailoring the porosity and pore size of electrospun synthetic human elastin scaffolds for dermal tissue engineering *Biomaterials* **32** 6729–36
[43] Chang H-I and Wang Y 2011 Cell responses to surface and architecture of tissue engineering scaffolds *Regenerative Medicine and Tissue Engineering—Cells and Biomaterials* (Rijeka: InTech)
[44] Ballester-Beltrán J, Rico P, Moratal D, Song W, Mano J F and Salmerón-Sánchez M 2011 Role of superhydrophobicity in the biological activity of fibronectin at the cell–material interface *Soft Matter* **7** 10803–11
[45] Erbil H Y 2003 Transformation of a simple plastic into a superhydrophobic surface *Science* **299** 1377–80
[46] Rockwood D N, Akins R E, Parrag I C, Woodhouse K A and Rabolt J F 2008 Culture on electrospun polyurethane scaffolds decreases atrial natriuretic peptide expression by cardiomyocytes *in vitro Biomaterials* **29** 4783–91
[47] Unsöld B *et al* 2014 Melusin protects from cardiac rupture and improves functional remodelling after myocardial infarction *Cardiovasc. Res.* **101** 97–107
[48] Fujio Y, Nguyen T, Wencker D, Kitsis R N and Walsh K 2000 AKT promotes survival of cardiomyocytes *in vitro* and protects against ischemia-reperfusion injury in mouse heart *Circulation* **101** 660–7
[49] Penna C, Brancaccio M, Tullio F, Rubinetto C, Perrelli M-G, Angotti C, Pagliaro P and Tarone G 2014 Overexpression of the muscle-specific protein, melusin, protects from cardiac ischemia/reperfusion injury *Basic Res. Cardiol.* **109** 418
[50] Sbroggiò M *et al* 2011 IQGAP1 regulates ERK1/2 and AKT signalling in the heart and sustains functional remodelling upon pressure overload *Cardiovasc. Res.* **91** 456–64
[51] Matsui T, Li L, del MonteF, Fukui Y, Franke T F, Hajjar R J and Rosenzweig A 1999 Adenoviral gene transfer of activated phosphatidylinositol 3′-kinase and Akt inhibits apoptosis of hypoxic cardiomyocytes *in vitro Circulation* **100** 2373–9
[52] Ricci C, Jong C J and Schaffer S W 2008 Proapoptotic and antiapoptotic effects of hyperglycemia: role of insulin signaling *Can. J. Physiol. Pharmacol.* **86** 166–72
[53] Sergeeva I A and Christoffels V M 2013 Regulation of expression of atrial and brain natriuretic peptide, biomarkers for heart development and disease *Biochim. Biophys. Acta* **1832** 2403–13
[54] Del R S, Cabiati M and Clerico A 2014 Natriuretic peptide system and the heart *Front. Horm. Res.* **43** 134–43
[55] McGrath M F and de Bold A J 2005 Determinants of natriuretic peptide gene expression *Peptides* **26** 933–43
[56] Ernest S, Jankowski M, Mukaddam-Daher S, Cusson J and Gutkowska J 1998 Altered regulation of natriuretic peptides in the rat heart by prenatal exposure to morphine *J. Physiol.* **506** 867–74
[57] Kohan D E, Rossi N F, Inscho E W and Pollock D M 2011 Regulation of blood pressure and salt homeostasis by endothelin *Physiol. Rev.* **91** 1–77
[58] Battistini B, Chailler P, D'Orléans-Juste P, Brière N and Sirois P 1993 Growth regulatory properties of endothelins *Peptides* **14** 385–99
[59] Suzuki T, Hoshi H and Mitsui Y 1990 Endothelin stimulates hypertrophy and contractility of neonatal rat cardiac myocytes in a serum-free medium *FEBS Lett.* **268** 149–51
[60] Ito H, Hirata Y, Hiroe M, Tsujino M, Adachi S, Takamoto T, Nitta M, Taniguchi K and Marumo F 1991 Endothelin-1 induces hypertrophy with enhanced expression of muscle-specific genes in cultured neonatal rat cardiomyocytes *Circ. Res.* **69** 209–15
[61] Carrier L, Boheler K R, Chassagne C, la Bastie de D, Wisnewsky C, Lakatta E G and Schwartz K 1992 Expression of the sarcomeric actin isogenes in the rat heart with development and senescence *Circ. Res.* **70** 999–1005
[62] Jiang H-K, Qiu G-R, Li-Ling J, Xin N and Sun K-L 2010 Reduced ACTC1 expression might play a role in the onset of congenital heart disease by inducing cardiomyocyte apoptosis *Circ. J.* **74** 2410–8
[63] Lompre A M, Nadal-Ginard B and Mahdavi V 1984 Expression of the cardiac ventricular alpha- and beta-myosin heavy chain genes is developmentally and hormonally regulated *J. Biol. Chem.* **259** 6437–46
[64] Gunning P, O'Neill G and Hardeman E 2008 Tropomyosin-based regulation of the actin cytoskeleton in time and space *Physiol. Rev.* **88** 1–35
[65] Tang W, Blair C A, Walton S D, Málnási-Csizmadia A, Campbell K S and Yengo C M 2016 Modulating beta-cardiac myosin function at the molecular and tissue levels *Front. Physiol.* **7** 659
[66] Touvron M, Escoubet B, Mericskay M, Angelini A, Lamotte L, Santini M P, Rosenthal N, Daegelen D, Tuil D and Decaux J-F 2012 Locally expressed IGF1 propeptide improves mouse heart function in induced dilated cardiomyopathy by blocking myocardial fibrosis and SRF-dependent CTGF induction *Dis. Models & Mech.* **5** 481–91
[67] Porter G A, Hom J, Hoffman D, Quintanilla R, de Mesy Bentley K and Sheu S-S 2011 Bioenergetics, mitochondria, and cardiac myocyte differentiation *Prog. Pediatr. Cardiol.* **31** 75–81

[68] Rosenblatt-Velin N, Lerch R, Papageorgiou I and Montessuit C 2004 Insulin resistance in adult cardiomyocytes undergoing dedifferentiation: role of GLUT4 expression and translocation *FASEB J.* **18** 872–4

[69] Lopaschuk G D and Jaswal J S 2010 Energy metabolic phenotype of the cardiomyocyte during development, differentiation, and postnatal maturation *J. Cardiovasc. Pharmacol.* **56** 130–40

[70] Chung S, Dzeja P P, Faustino R S, Perez-Terzic C, Behfar A and Terzic A 2007 Mitochondrial oxidative metabolism is required for the cardiac differentiation of stem cells *Nat. Clin. Pract. Cardiovasc. Med.* **4** (Suppl 1) S60–7

[71] Cho Y M, Kwon S, Pak Y K, Seol H W, Choi Y M, Park D J, Park K S and Lee H K 2006 Dynamic changes in mitochondrial biogenesis and antioxidant enzymes during the spontaneous differentiation of human embryonic stem cells *Biochem. Biophys. Res. Commun.* **348** 1472–8

[72] St John J C, Ramalho-Santos J, Gray H L, Petrosko P, Rawe V Y, Navara C S, Simerly C R and Schatten G P 2005 The expression of mitochondrial DNA transcription factors during early cardiomyocyte *in vitro* differentiation from human embryonic stem cells *Cloning Stem Cells* **7** 141–53